Shock Waves (2015) 25:329–345
DOI 10.1007/s00193-014-0539-y

ORIGINAL ARTICLE

Numerical simulations of a shock interacting with successive interfaces using the Discontinuous Galerkin method: the multilayered Richtmyer–Meshkov and Rayleigh–Taylor instabilities

M. T. Henry de Frahan · P. Movahed · E. Johnsen

Received: 28 February 2014 / Revised: 23 June 2014 / Accepted: 13 October 2014 / Published online: 14 November 2014

Abstract In this work, we investigate the growth of interface perturbations following the interaction of a shock wave with successive layers of fluids. Using the Discontinuous Galerkin method, we solve the two-dimensional multifluid Euler equations. In our setup, a shock impacts up to four adjacent fluids with perturbed interfaces. At each interface, the incoming shock generates reflected and transmitted shocks and rarefactions, which further interact with the interfaces. By monitoring perturbation growth, we characterize the influence these instabilities have on each other and the fluid mixing as a function of time in different configurations. If the third gas is lighter than the second, the reflected rarefaction at the second interface amplifies the growth at the first interface. If the third gas is heavier, the reflected shock decreases the growth and tends to reverse the Richtmyer–Meshkov instability as the thickness of the second gas is increased. We further investigate the effect of the reflected waves on the dynamics of the small scales and show how a phase difference between the perturbations or an additional fluid layer can enhance growth. This study supports the idea that shocks and rarefactions can be used to control the instability growth.

Keywords Richtmyer–Meshkov instability · Rayleigh–Taylor instability · Multifluid · Multilayered · Discontinuous Galerkin

Communicated by D. Ranjan.

This paper is based on work that was presented at the 29th International Symposium on Shock Waves, Madison, Wisconsin, USA, July 14–19, 2013.

M. T. Henry de Frahan (✉) · P. Movahed · E. Johnsen
Mechanical Engineering Department, University of Michigan, Ann Arbor, MI 48109, USA
e-mail: marchdf@umich.edu

1 Introduction

Hydrodynamic instabilities play important roles in high-energy-density physics (HEDP) problems [14], such as in inertial confinement fusion (ICF) [27] and supernova collapse [23]. The Richtmyer–Meshkov instability (RMI) occurs in flows where a shock interacts with a perturbed interface between two fluids of different densities. At interfaces, the incoming shock deposits baroclinic vorticity that drives the perturbation growth [5]. ICF capsules and supernovae both consist of concentric layers of different materials in a spherical geometry. As a result of high-energy lasers or star collapse, shocks are generated and interact with these multiple layers. The interfaces, already unstable to the shock interaction, further experience accelerations due to the converging geometry [16]. As a result, situations in which a heavy material is accelerated into a light material are also Rayleigh–Taylor (RT) [36] unstable. These hydrodynamic instabilities govern the subsequent hydrodynamics of the ICF capsule and the supernovae. In ICF capsules, mixing between the outer ablator shell and the inner fuel is one of the dominant limitations preventing fusion burn [25].

The canonical RMI, consisting of a single planar shock wave interacting with a single planar interface separating two fluids, has been studied extensively in the past, both experimentally [11,21,29,37] and numerically [20,22,26,31,34]. While some of these studies have considered late-time mixing, most have focused on the early time dynamics. Furthermore, little attention has been given to shocks interacting with multiple interfaces, a set-up relevant to ICF and supernova collapse. Most of the research involving multiple layers focused on gas curtains, as in [4,28,35], which consider a thin layer of fluid within another fluid.

Systematic studies involving shocks interacting with three or more different fluids have yet to be performed. Following

the interaction of a wave with an interface, a reflected and a transmitted wave are produced. Depending on the acoustic impedance of each fluid and the incoming wave, the waves resulting from this interaction may be compressions or rarefactions. For systems with many layers, many such interactions occur, and whether the growth of a given perturbed interface is enhanced or inhibited depends on the direction of the baroclinic vorticity deposited by all the waves. Thus, although perturbations are expected to grow due to the RMI of the incoming shock, this growth may be inhibited or enhanced by rarefactions (i.e., transient acceleration fields due to a varying pressure) depending on whether the system is RT-stable. Furthermore, the growth may be enhanced by additional RMI due to subsequent shock interactions. Eventually, these instabilities contribute to mixing between the layers.

Our objective is to use numerical simulations to investigate the interaction of a shock wave with successive perturbed interfaces, and specifically Richtmyer–Meshkov (due to shocks) and Rayleigh–Taylor (due to rarefactions) growth. We are interested in determining whether perturbation growth is enhanced or inhibited due to the fluid properties (acoustic properties of the gases and separation). We consider multiple adjacent ideal gases separated by single-mode perturbed interfaces. We use the high-order accurate Discontinuous Galerkin method to solve the multifluid Euler equations [18,19]. Using two-dimensional simulations, we analyze the effects of the shocks, rarefactions, and the separation distance on the mixing between the three fluids. The manuscript is organized as follows. First, the physical model and numerical model are presented, followed by a validation study. We then investigate the perturbations growth for our baseline problem (a shock interacting with three adjacent gases), and quantify the mixing and small-scales dynamics. We close with a discussion of phase differences between the perturbations and the addition of a fourth fluid layer.

2 Physical model and numerical method

We consider the two-dimensional Euler equations,

$$\frac{\partial \rho}{\partial t} + \frac{\partial}{\partial x_j}\left(\rho u_j\right) = 0, \tag{1a}$$

$$\frac{\partial (\rho u_i)}{\partial t} + \frac{\partial}{\partial x_j}\left(\rho u_i u_j + p\delta_{ij}\right) = 0, \tag{1b}$$

$$\frac{\partial E}{\partial t} + \frac{\partial}{\partial x_j}\left[u_j(E+p)\right] = 0, \tag{1c}$$

where ρ is the density, u_i is the velocity, $E = \rho e + \frac{1}{2}\rho u_i u_i$ is the total energy, e is the internal energy, p is the pressure and δ_{ij} is the Kronecker delta. The system is closed by the ideal gas equation of state relating the internal energy to the pressure, $\rho e = \frac{p}{\gamma - 1}$, where γ is the specific heats ratio. Here, physical diffusion processes are neglected since we consider high Reynolds number flows.

To avoid spurious pressure oscillations in flows with variable γ, it is necessary to solve an additional non-conservative transport equation for γ to capture interfaces [1],

$$\frac{\partial}{\partial t}\left(\frac{1}{\gamma - 1}\right) + u_j \frac{\partial}{\partial x_j}\left(\frac{1}{\gamma - 1}\right) = 0. \tag{2}$$

We extended this approach to the Discontinuous Galerkin method [18,19]. The Discontinuous Galerkin method [6–10] is a numerical method for solving partial differential equations which combines the advantages of the finite element and finite volume methods. In contrast with previous RMI studies using finite difference and finite volume methods [20,22,26,28,34], the numerical solution is represented in each computational cell of the domain with high-order polynomial basis functions. The method is therefore high-order accurate and is superconvergent in the cell averages at a rate of $2N+1$ [2,3], where $N+1$ is the number of basis function in each cell. The method's compact stencil, i.e., cells communicate only with their direct neighbors, enables a highly scalable implementation for parallel architectures. Additionally, the Discontinuous Galerkin method is naturally amenable to unstructured grids. At cell interfaces, a Riemann solver is implemented to calculate the fluxes between the cells. In this paper, the cell fluxes are calculated by the approximate Riemann solver of Roe [33]. Additionally, a limiting procedure is required to avoid solution oscillations at flow discontinuities. We use a non-oscillatory, conservative, and high-order accurate limiting procedure based on hierarchical reconstruction, which has been suitably modified to prevent spurious pressure oscillations [19]. Solution limiting is performed gradually and hierarchically from the highest polynomial degree to the lowest to retain as much of the high-order accuracy of the method as possible. In contrast with other limiters, e.g., [7], the present limiter does not reduce the solution to first order in the flow domain but is $(N+1)$st order accurate. At discontinuities, the scheme reduces to first order, as do all finite volume, finite difference, and Discontinuous Galerkin method shock-capturing schemes. The system is evolved in time using the standard explicit fourth-order Runge-Kutta method [24] with a Courant number of 0.5.

Taking advantage of the method's compact stencil [7], a highly parallel version of the method on graphics processing units (GPU) is implemented. This allows for simulations completing approximately two orders of magnitude faster than on a single CPU. The high-resolution simulations in this paper completed in approximately one hour. The simulations were performed on GPUs at the Flux cluster at the Center for Advanced Computing at the University of Michi-

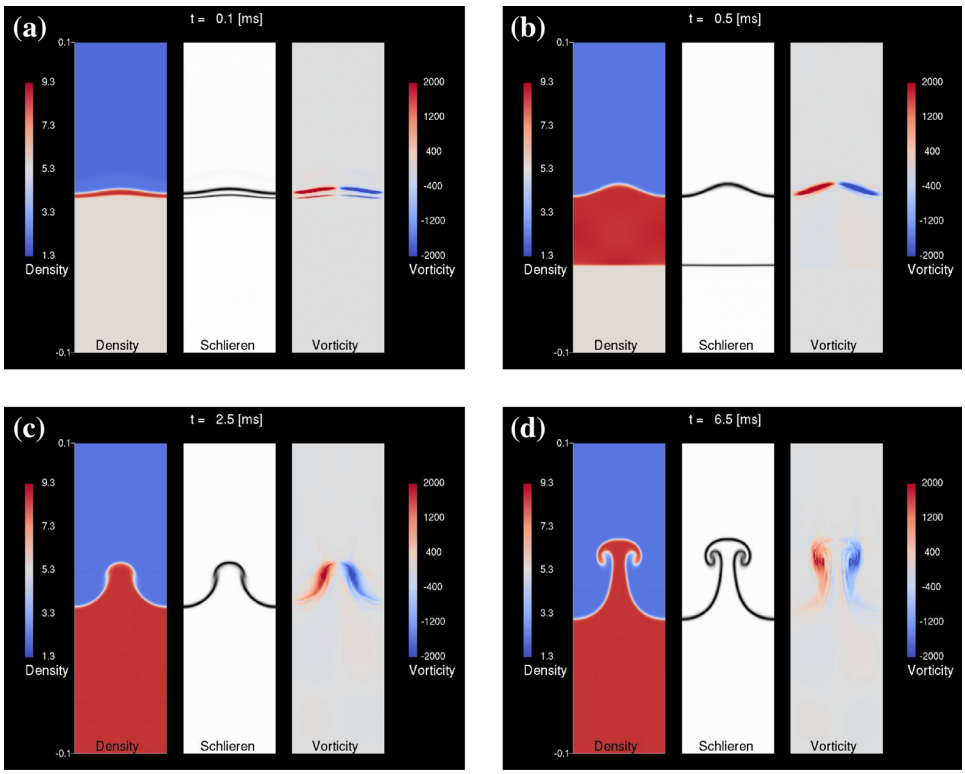

Fig. 1 Density (*left*), density gradient (numerical schlieren, *middle*), and vorticity fields (*right*) for the single-interface RMI. Shock wave moving downwards. Air (*top*)–SF_6 (*bottom*). **a** $t = 0.1$ ms. **b** $t = 0.5$ ms. **c** $t = 2.5$ ms. **d** $t = 6.5$ ms

gan. Mesh generation and post-processing visualization were carried out with Gmsh, a three-dimensional finite element mesh generator with built-in pre- and post-processing facilities [15]. Our code has been used previously to simulate HEDP experiments of blast-wave-driven shear flow [13].

3 Single-interface RMI validation

We use the single-mode RMI experiments of [11] to validate our numerical method. Two gases, air and SF_6, lie in a shocktube at atmospheric pressure, and the interface between the two is sinusoidally perturbed. The properties of air are $\rho_{air} = 1.351\,\text{kg/m}^3$, $\gamma_{air} = 1.276$, and those of SF_6 are $\rho_{SF_6} = 5.494\,\text{kg/m}^3$, $\gamma_{SF_6} = 1.093$ [26]. The initial amplitude and wavelength of the interfacial perturbations are $a_0 = 0.183$ cm and $\lambda = 5.933$ cm, respectively. The mean air-SF_6 interface is initially at $y = 0$. A Mach 1.21 shock initialized in air impinges upon the perturbed interface, thereby initiating the RMI growth.

For these simulations, the domain is one perturbation wavelength wide in the x-direction and 20 cm long in the y-direction. The boundaries are periodic on the sides, and we impose non-reflecting boundary conditions, modeled as zero gradient boundary conditions, at the entrance and exit of the shock tube. The domain is discretized uniformly in x and y. The number of cells per wavelength is 128. We use a linear polynomial basis ($N = 1$) for the Discontinuous Galerkin method, resulting in third-order accuracy in smooth regions. An exponential diffusion function is used to initialize a thermodynamically consistent diffuse interface between the gases [26], with a thickness set to 0.5 cm. To avoid a large spatial domain, we add a constant upward velocity calculated from an exact Riemann solver so that the post-shock upward mean velocity is zero and the interfaces remain in the domain. As we are interested in the mixing layer width, the perturbation amplitudes in this paper are measured as half the difference between the maximum and the minimum y-position of the perturbation. The perturbation location is found by taking the 0.5 contour level of the mass fraction field. This measure of the amplitude does not take into account the phase of the perturbation.

Upon interaction with the interface, the shock generates baroclinic vorticity due to the misalignment of the density and pressure gradients (Fig. 1a, b). As a result, the perturbed interface grows in time, leading to bubbles of light fluid penetrating the heavier one, and spikes of heavy fluid penetrating the lighter one (Fig. 1c, d). Figure 2 compares the early-time experimental growth (before reshock, at 6.6 ms in the experiment) of the instability with the simulation growth at different resolutions. As the grid is refined, the results (amplitude) converge in an integral sense, with good agreement with the experimental data. The numerical results in

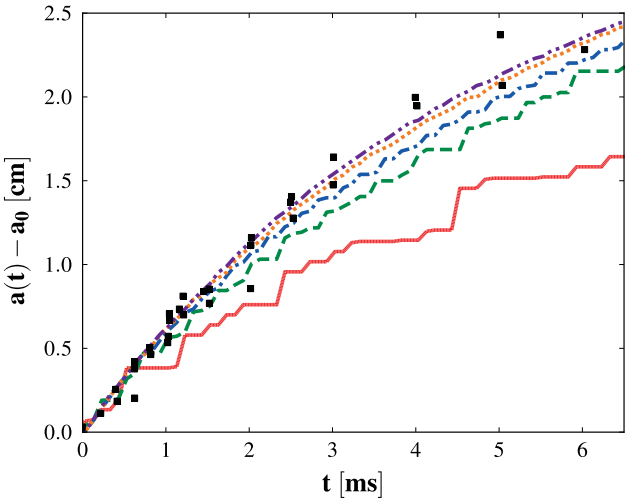

Fig. 2 Instability growth versus time for the single-interface RMI. *Black squares* experimental data from [11]. *Lines* simulation results at 16 (*solid red*), 32 (*dash green*), 64 (*dash-dot blue*), 128 (*dot orange*), and 256 (*dash-dot-dot purple*) cells per wavelength

this paper were performed using the grid with 128 cells per wavelength.

4 Shock interaction with two successive interfaces

Our baseline problem consists of a shock interacting successively with two interfaces separated by a distance h. Our set-up can be described as three adjacent gases (A, B, and C) with interfaces initially perturbed with the same single mode, and a shock initialized in the first gas (Fig. 3). For comparison with single-interface RMI studies [11], we choose air for gas A, SF_6 for gas B, and a shock Mach number of 1.21. The goal is to understand how the physics depend on the nature of the third gas (heavy or light—see Table 1). In particular, we study the effect of increasing the thickness of gas B (i.e., the distance separating gas A from gas C) measured by the non-dimensional distance $\frac{h}{\lambda}$, where λ is the perturbation wavelength. We also change the density of gas C, Table 1, to create either a reflected rarefaction or shock at the second interface. The nominal case (no gas C) corresponds to the experiment in [11] with no reshock, as in Sect. 3.

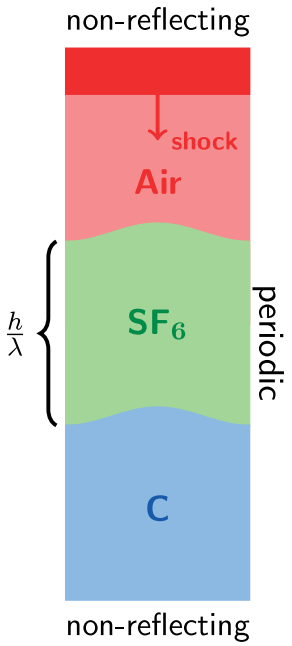

Fig. 3 Baseline multi-layered problem setup

Table 1 Relevant properties for the third gas (C)

Case	Gas A	Gas B	ρ_C [kg/m^3]	γ_C
Nominal [11]	Air	SF_6	–	–
1	Air	SF_6	0.178	5/3
2	Air	SF_6	10	5/3

4.1 Light third gas

We first consider a third gas (C), whose properties correspond to helium and is lighter than SF_6 (B). Figure 4 shows the waves produced during the process in an $x - t$ diagram, and Fig. 5 provides a qualitative illustration of the effect these waves have on the dynamics of the interfaces through contours of density, density gradient (displayed as a numerical schlieren image) and vorticity. When the shock interacts with the first interface and deposits baroclinic vorticity (Fig. 5a), a transmitted and a reflected shock are created; the reflected

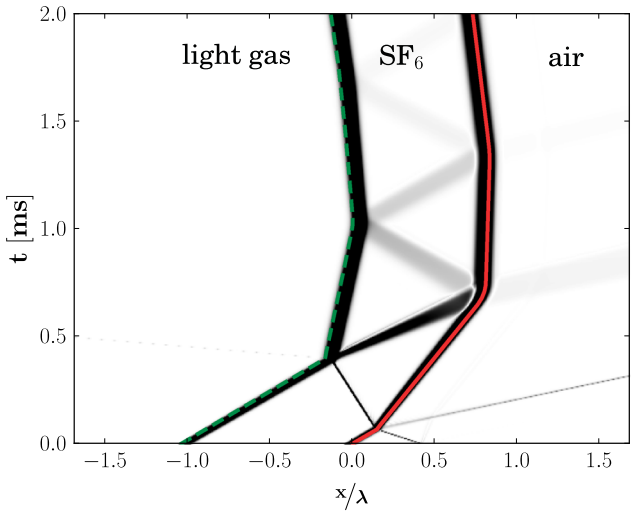

Fig. 4 Wave diagram from a one-dimensional simulation for the baseline problem with a light third gas (initial shock coming from the right, $\frac{h}{\lambda} = 1$). *Solid red* air-SF_6 interface; *dashed green* SF_6-light third gas interface

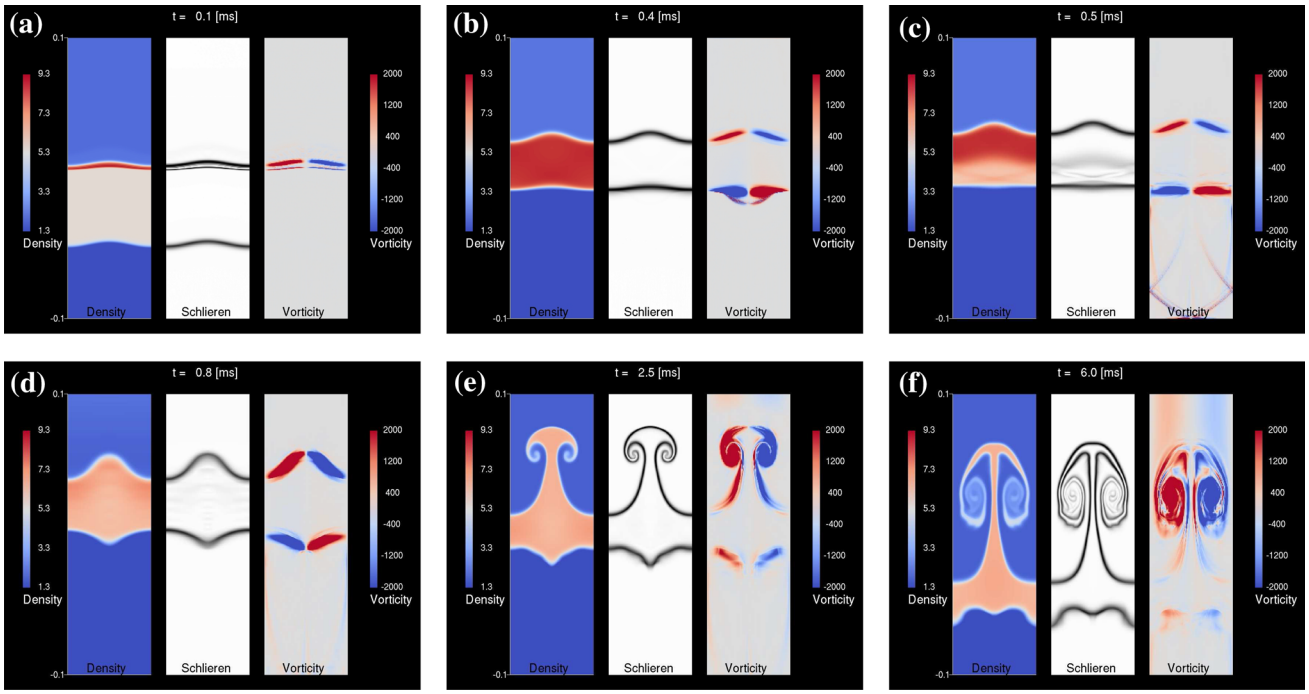

Fig. 5 Density (*left*), density gradient (numerical schlieren, *middle*), and vorticity (*right*) fields for the baseline problem with a light third gas and $\frac{h}{\lambda} = 1$. Shock wave moving downwards. Air (*top*)–SF_6 (*middle*)–light gas (*bottom*). **a** $t = 0.1$ ms. **b** $t = 0.4$ ms. **c** $t = 0.5$ ms. **d** $t = 0.8$ ms. **e** $t = 2.5$ ms. **f** $t = 6.5$ ms

shock eventually leaves the domain. The transmitted shock then impinges upon the second interface, and deposits vorticity (Fig. 5b). From this latter interaction, a reflected rarefaction and another transmitted shock, which eventually leaves the domain, are produced (Fig. 5c). The reflected rarefaction propagates back towards the first interface and interacts with the evolving instability (Fig. 5c). Given the sign of the vorticity already present along the interface due to the first shock interaction, this rarefaction further increases the vorticity (Fig. 5d). Alternately, this process can be understood as an accelerated interface in an RT-unstable configuration due to the transient passage of the rarefaction. This overall process thus initiates two spikes moving in opposite directions: one into gas A (produced by the incoming shock and reflected rarefaction) and the other into gas C (due to the transmitted shock). The nonlinear evolution of the perturbations is visible in Fig. 5e, f. Eventually the reflected waves diminish in strength and do not affect the dynamics of the interfaces anymore.

The perturbation growth at both interfaces is shown in Fig. 6 for different non-dimensional spacings $\frac{h}{\lambda}$ between the interfaces. We start by considering the first interface (Fig. 6a). Until the reflected rarefaction reaches it, the growth of the first interface is that of the nominal case. A transition immediately follows where the growth is nonlinear and increases dramatically. This behavior is caused by rarefactions reflected from the second interface and interacting with the first. These rarefactions deposit vorticity at the first interface in the same direction as the initial shock, thus amplifying the initial growth. These waves have the effect of accelerating the heavy fluid into the light fluid, an unstable configuration that leads to transient RT growth. As $\frac{h}{\lambda}$ is increased, these waves reach the first interface at later times. As a result, the perturbation amplitude is larger when the rarefaction reaches the interface, thus enhancing the baroclinic vorticity generation. Additionally, the rarefactions have spread more, increasing the interaction time with the interface. In this RT unstable set-up, the acceleration is applied for a longer time. For these two reasons, the growth rate of the first interface increases with increasing $\frac{h}{\lambda}$. After $t > 3$ ms, the growth rate is constant; it is higher for larger values of $\frac{h}{\lambda}$ due to the larger amplitude at the time of interaction. By then, the reflected and transmitted waves have left the domain or decreased in amplitude such that their effect on the growth is negligible.

The morphology and evolution of the second interface is different and strongly depends on $\frac{h}{\lambda}$ (Fig. 6b). In the case of $\frac{h}{\lambda} = 0.5$, a single SF_6 spike moves downward while the air and helium interfaces start interacting on the sides of the spike, (Figs. 6b, 7). The evolution of this interface for $\frac{h}{\lambda} = 1.5$ is very different. An initial central SF_6 spike moves downward. The interface then experiences a phase reversal following interaction with the compression generated by the

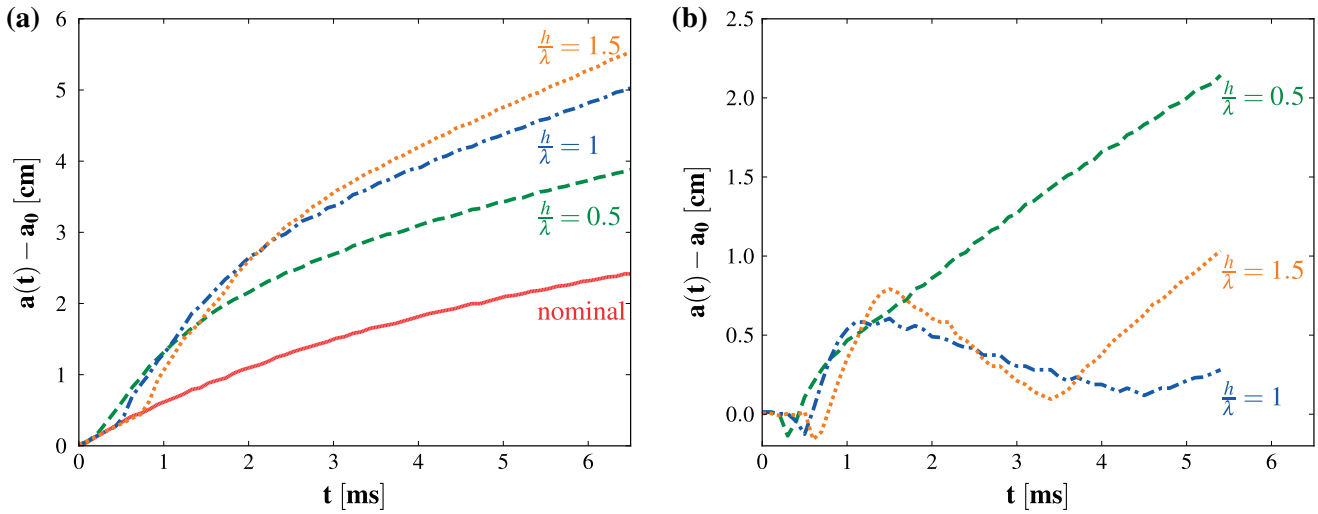

Fig. 6 Interface growth versus time for the baseline problem with a light third gas for different thicknesses of gas B. **a** Air-SF_6 interface. **b** SF_6-light third gas interface

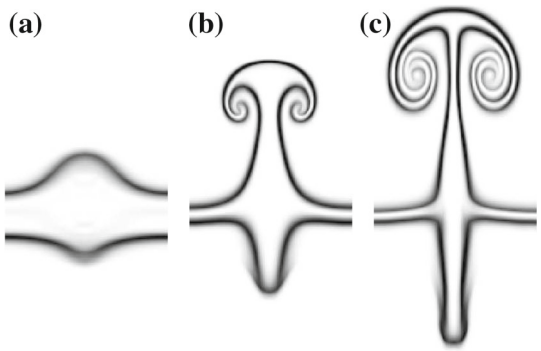

Fig. 7 Density gradient (numerical schlieren) for the baseline problem with a light third gas for $\frac{h}{\lambda} = 0.5$. **a** $t = 0.6$ ms. **b** $t = 2.5$ ms. **c** $t = 5$ ms

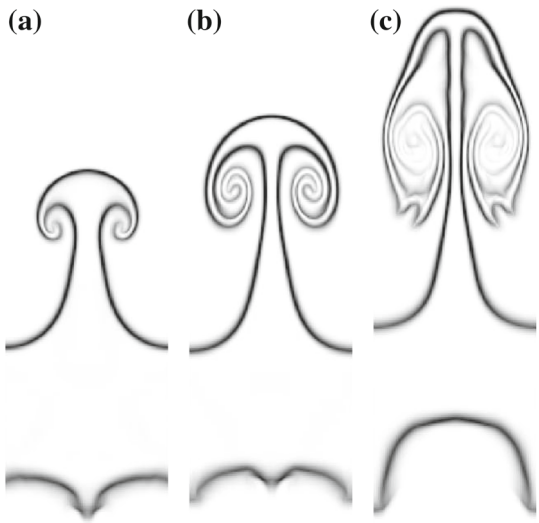

Fig. 8 Density gradient (numerical schlieren) for the baseline problem with a light third gas for $\frac{h}{\lambda} = 1.5$. **a** $t = 2.5$ ms. **b** $t = 3.8$ ms. **c** $t = 6.5$ ms

reflection of the rarefaction at the first interface (Figs. 6b, 8). This effect is less important for the $\frac{h}{\lambda} = 1$ case, Fig. 6b. At later times, interface proximity effects affect the flow dynamics by enabling or preventing the phase reversal. In addition, reflecting waves in the SF_6 interact with higher amplitude perturbations as the separation distance increases, thereby increasing the baroclinic vorticity generation.

4.2 Heavy third gas

We now consider a third gas (C), which is heavier than SF_6 (B). Figure 9 shows the different transmitted and reflected waves in an $x - t$ diagram, and Fig. 10 provides a qualitative illustration of the effect these waves have on the dynamics of the interfaces. In this set-up, the transmitted shock from the first interface leads to a reflected and transmitted shock at the second interface (Fig. 10a). Upon interaction with the evolving RMI at the first interface, the reflected shock decreases the amount of vorticity at the first interface by depositing vorticity in the opposite direction (Fig. 10b). Both perturbations grow in the same direction, with the first spike moving slowly into gas A (Fig. 10c).

Figure 11a illustrates the growth of the RMI at the first interface for different $\frac{h}{\lambda}$. The growth follows that of the nominal case until the reflected shock from the second interface reaches it. The growth and growth rate decrease thereafter, more so as $\frac{h}{\lambda}$ increases. Because the reflected shock moves from a dense to a less dense gas, the reflected shock deposits vorticity in the opposite direction as the initial shock. Further amplifying this effect, the greater distance implies that

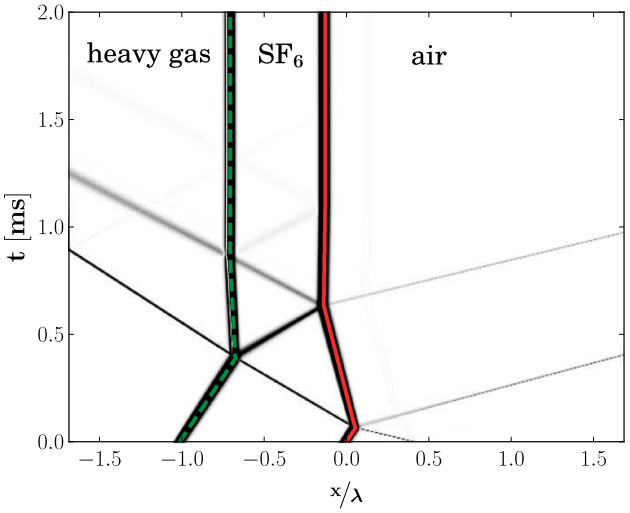

Fig. 9 Wave diagram from a one-dimensional simulation for the baseline problem with a heavy third gas (initial shock coming from the right, $\frac{h}{\lambda} = 1$). *Solid red* air-SF_6 interface; *dashed green* SF_6-heavy third gas interface

the perturbation has grown more before interacting with the reflected shock. As $\frac{h}{\lambda}$ increases, the growth rate becomes negative, indicating a phase reversal of the RMI. Although the set-up is analogous, the growth of the perturbation amplitude does not increase as significantly as in experiments with reshock [11] because of the weaker transmitted shock and smaller interface perturbations at the time of interaction, as in the previous section. The monotonic attenuation in the amplitude with increasing $\frac{h}{\lambda}$ is most likely limited to cases when the second shock interacts with the interface before the perturbation becomes nonlinear. It is to be expected that a reflected shock interacting with a nonlinear interface leads to a large increase in the perturbation amplitude and increased mix. For $\frac{h}{\lambda} = 1.5$, we observe "freeze-out" of the growth due to the multiple wave interactions [28]. This supports the idea that shell thickness and shock timing could be used advantageously to minimize the amount of mix and spike penetration in ICF capsules [14]. The second interface (between the SF_6 and the heavy gas) exhibits continuous growth and no phase

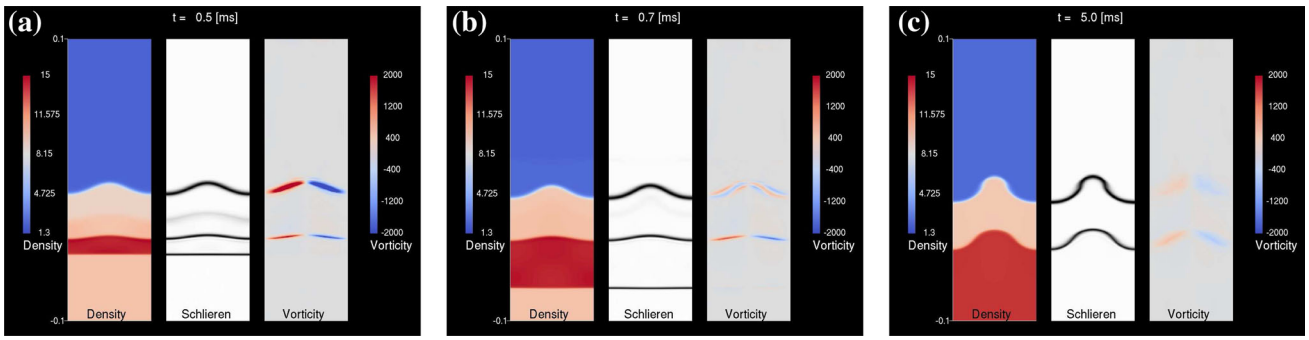

Fig. 10 Density (*left*), density gradient (numerical schlieren, *middle*), and vorticity (*right*) fields for the baseline problem with a heavy third gas and $\frac{h}{\lambda} = 1$. **a** $t = 0.5$ ms. **b** $t = 0.7$ ms. **c** $t = 5$ ms

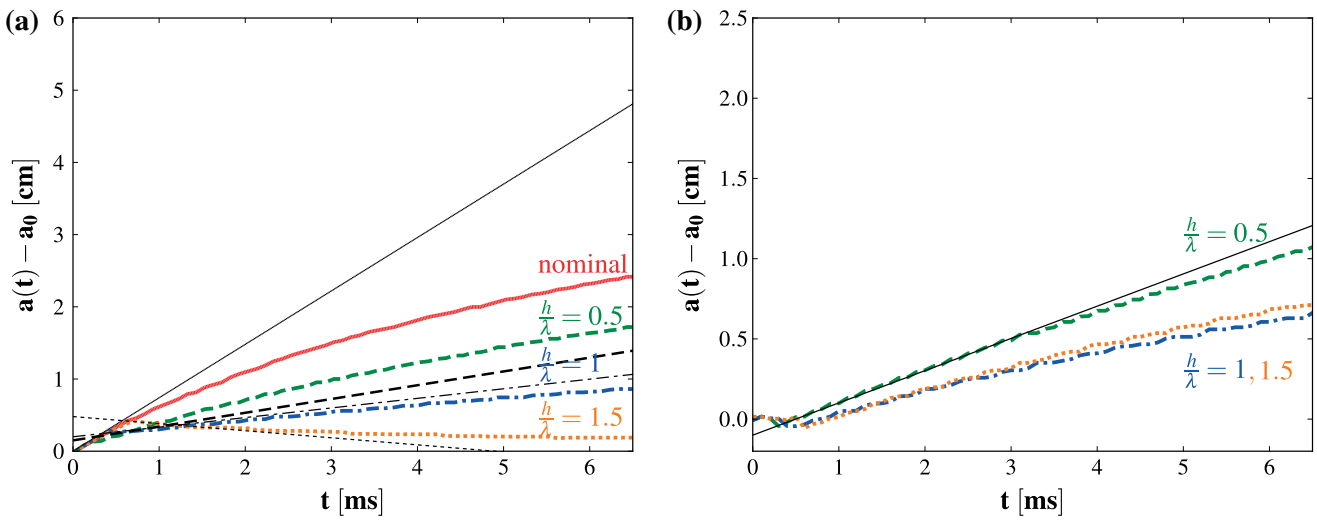

Fig. 11 Interface growth versus time for the baseline problem with a heavy third gas for different thicknesses of gas B. *Black lines* impulsive model [32] for the growth after the interaction with the first shock and the reflected shock. **a** Air-SF_6 interface. **b** SF_6-heavy third gas interface

Table 2 Density, velocity, and pressure from solving the shock interactions with an exact Riemann solver for the baseline problem with a heavy third gas (SI units)

Interaction	Air	SF_6	Heavy third gas
Shock at 1st interface			
ρ	1.87	5.5	10
u	103.6	0	0
p	1.52×10^5	10^5	10^5
Transmitted shock at 2nd interface			
ρ	2.07	9.02	10
u	71.75	71.75	0
p	1.72×10^5	1.72×10^5	10^5
Reflected shock from 2nd interface at 1st interface			
ρ	2.07	10.1	14.79
u	71.75	55.43	55.43
p	1.72×10^5	1.95×10^5	1.95×10^5
Post-shock refraction			
ρ	2.21	9.74	14.79
u	50.21	50.21	55.43
p	1.87×10^5	1.87×10^5	1.95×10^5

reversal (Fig. 11b). The growth rates are similar since the subsequent waves interact weakly with this interface after the transmitted shock interaction.

In Fig. 11a, we compare the impulsive model [32] to the initial growth rate of the instability and the growth rate after the interaction with the reflected shock. The impulsive model growth rate is given by

$$\frac{\mathrm{d}a}{\mathrm{d}t} = k\Delta u A^+ a_0^+, \tag{3}$$

where $a(t)$ is the perturbation amplitude, a_0^+ is the post-shock amplitude, k is the perturbation wave number, $A^+ = (\rho_1^+ - \rho_2^+)/(\rho_1^+ + \rho_2^+)$ is the post-shock Atwood number, and Δu is the velocity jump at the interface following shock refraction. For the nominal case, the growth rate is 7.4 m/s [26]. We solve three Riemann problems using an exact Riemann solver to calculate the numerical values of A^+ and Δu to determine the growth due to the reflected shock from the second interface: (i) the initial shock interacting with the first interface; (ii) the transmitted shock interacting with the second interface; and (iii) the reflected shock from the second interface interacting with the first interface. The various states of the gases are reported in Table 2. The a_0^+ is measured from two-dimensional simulations right after shock refraction: $a_0^+ = 0.38$ cm for $\frac{h}{\lambda} = 0.5$, $a_0^+ = 0.42$ cm for $\frac{h}{\lambda} = 1$, and $a_0^+ = 0.58$ cm for $\frac{h}{\lambda} = 1.5$. We subtract the growth rate due to the reflected shock from the initial nominal growth rate to obtain the growth after reflected shock interaction: $\frac{\mathrm{d}a}{\mathrm{d}t} = 5.49$ m/s for $\frac{h}{\lambda} = 0.5$, $\frac{\mathrm{d}a}{\mathrm{d}t} = 6.07$ m/s for $\frac{h}{\lambda} = 1$, and $\frac{\mathrm{d}a}{\mathrm{d}t} = 8.38$ m/s for $\frac{h}{\lambda} = 1.5$. From Fig. 11a, the impulsive model accurately predicts the initial growth rates after both shock interactions and deviates from the simulation results at later times, as expected. In Fig. 11b, the impulsive model agrees well with the initial growth rate of the second interface for the three separation distances.

5 Fluid mixing

Although physical diffusion is neglected, we are interested in mixing between the different fluids through fluid entrainment and dispersion, i.e., at large and intermediate scales. For analysis purposes, we use metrics analogous to those used to measure chemical mixing. We quantify the amount of mixing between the fluids using two different approaches.

We first define the mix between fluid A and B as

$$M_{AB} = \int_S \rho^2 Y_A Y_B \,\mathrm{d}S, \tag{4}$$

where $Y_{(i)}$ is the mass fraction of fluid i. This equation represents the total reaction rate in a chemical reaction between fluid A and B with a temperature invariant reaction rate [17,30,38]. The total mix, M, in the system is defined as

$$M = M_{AB} + M_{BC} + M_{AC}, \tag{5}$$

where fluid A is the air, fluid B is the SF_6, and fluid C is the third gas.

To study mix without the effect of the density difference between the first and second interface and to distinguish between mixed gas and unmixed entrained gas, we use the ratio of the total chemical product formed by the mixing fluids and the entrainment length [12]. The chemical product formed by a chemical reaction between fluid A and B limited by the lean reactant and, with a stoechiometric coefficient of 0.5, is

$$Y_{AB} = \begin{cases} 2Y_A, & \text{if } Y_A \leq 0.5, \\ 2Y_B, & \text{if } Y_B < 0.5. \end{cases} \tag{6}$$

The total chemical product in the system from this reaction is equal to

$$P_{AB} = \int_{-\infty}^{\infty} \langle Y_{AB} \rangle \,\mathrm{d}y, \tag{7}$$

where $\langle\cdot\rangle$ denotes the average in the (transverse) x-direction. The maximum chemical product possible resulting from complete mixing (homogenization) of the two fluids in each y-plane is

$$h_{AB} = \int_{-\infty}^{\infty} Y_{AB}(\langle Y_A \rangle, \langle Y_B \rangle) \,\mathrm{d}y. \tag{8}$$

This quantity is the entrainment length [12], which is also a measure of mixing layer thickness. Another measure of mixing can be defined as

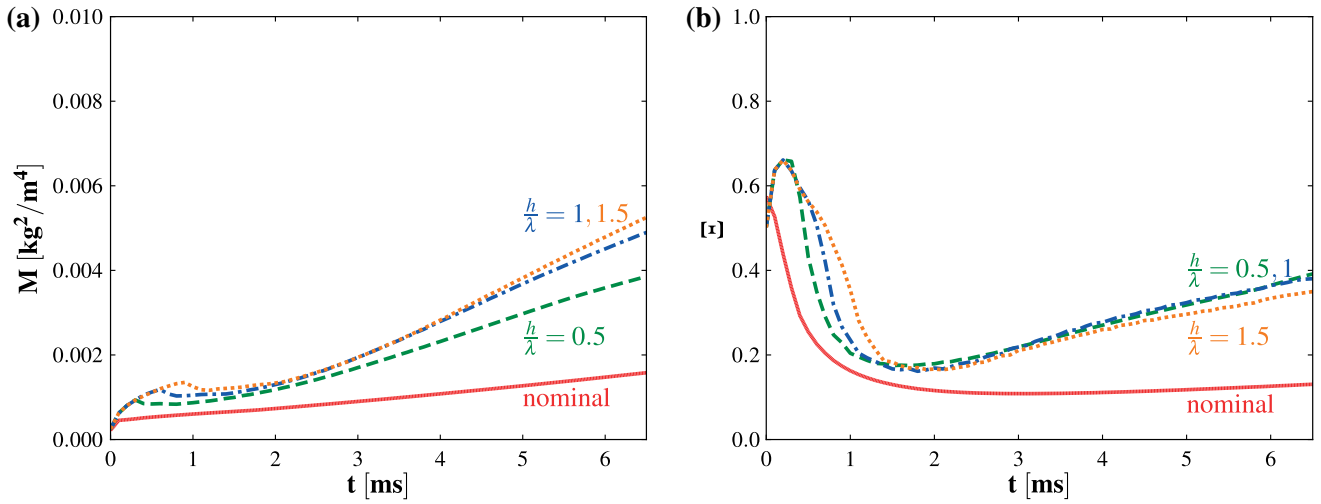

Fig. 12 Mixing metrics versus time for the baseline problem with a light third gas for different thicknesses of gas B. **a** M. **b** Ξ

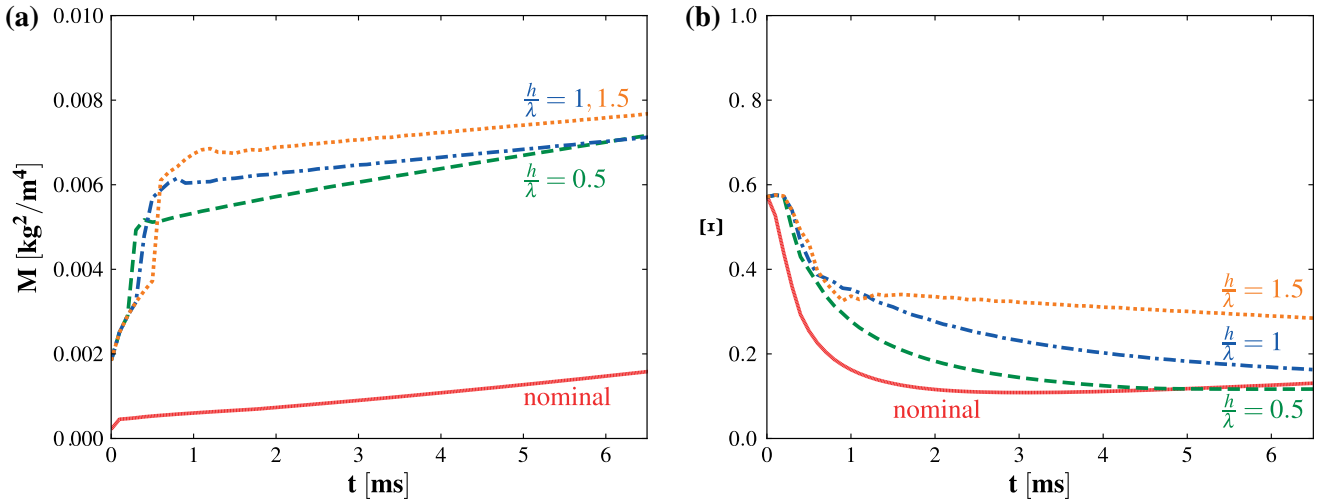

Fig. 13 Mixing metrics versus time for the baseline problem with a heavy third gas for different thicknesses of gas B. **a** M. **b** Ξ

$$\Xi_{AB} = \frac{P_{AB}}{h_{AB}}. \tag{9}$$

This quantity is close to unity when the fluids are completely mixed, i.e., $P_{AB} \approx h_{AB}$, and close to zero when the fluids are segregated, i.e., $P_{AB} \ll h_{AB}$. It, therefore, distinguishes between mixed fluids and unmixed entrained fluids. We quantify the total mixing in the system as

$$\Xi = \frac{P_m}{h_m} = \frac{P_{AB} + P_{BC} + P_{AC}}{h_{AB} + h_{BC} + h_{AC}}. \tag{10}$$

For the light third gas case, M is shown in Fig. 12a. M is larger for the light third gas case than the nominal case. This is due to the large perturbation growth from the RT-unstable phase driven by the rarefactions and the presence of two interfaces mixing. M increases as $\frac{h}{\lambda}$ increases because of the high growth of the first interface for larger $\frac{h}{\lambda}$. Because of the high density at the air-SF_6 interface relative to that at the SF_6-light gas interface, M mostly measures the mixing of the air with the SF_6. Figure 12b shows the temporal evolution of Ξ. This quantity starts at a high value because the perturbed interfaces are initially diffuse and no small-scale features are present. The decrease in Ξ, after the shock and rarefaction interactions, is due to the entrainment of the fluids that do not mix on these time scales as the mixing region width increases. As time increases, the mixing between the fluids increases, as does Ξ. As $\frac{h}{\lambda}$ is varied, Ξ does not change significantly, indicating that an increase in entrainment length is balanced with a corresponding increase in unmixed interpenetrating fluids. The mix between the first and third gases, M_{AC} and Ξ_{AC}, is essentially zero for all cases.

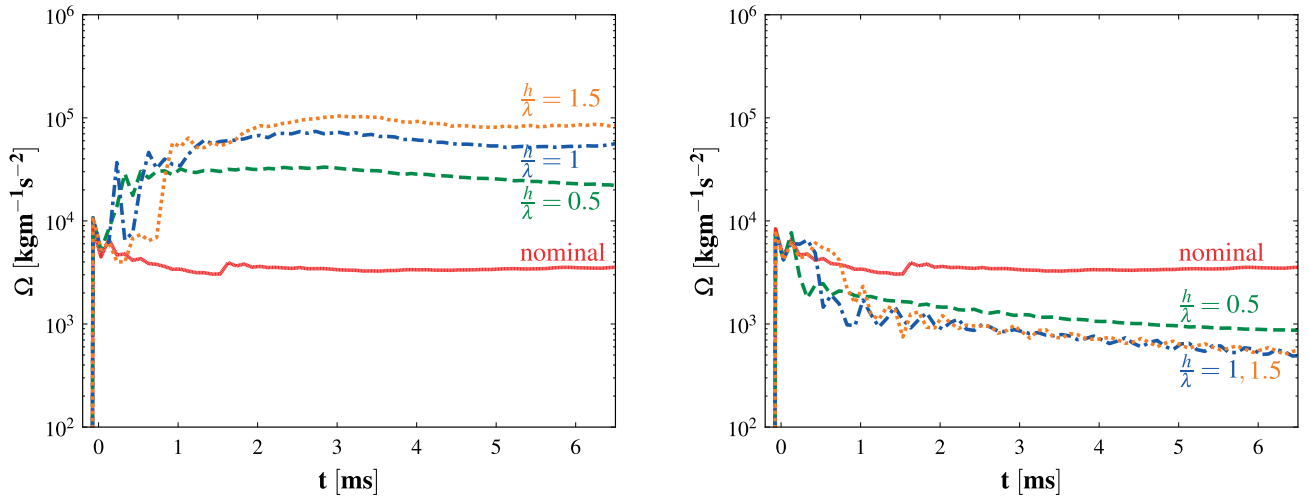

(a) Light third gas. **(b)** Heavy third gas.

Fig. 14 Enstrophy versus time for the baseline problem for different thicknesses of gas B. **a** Light third gas. **b** Heavy third gas

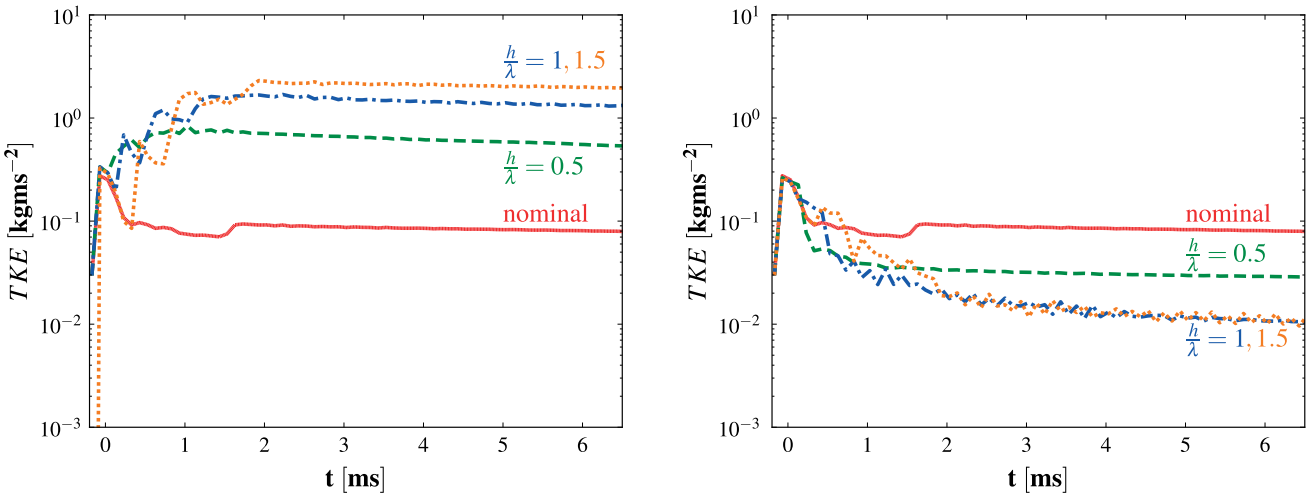

(a) Light third gas. **(b)** Heavy third gas.

Fig. 15 Turbulent kinetic energy versus time for the baseline problem for different thicknesses of gas B. **a** Light third gas. **b** Heavy third gas

For the heavy third gas case, because of the density weighing, M is dominated by the mixing at the second interface (Fig. 13a). As $\frac{h}{\lambda}$ increases, the transmitted shock reaches the second interface later in time. By then, the second interface has stretched more before being shocked. The increased length of this diffusion layer results in increased M with $\frac{h}{\lambda}$ after the transmitted shock interaction. M is almost constant after the shock interaction because there is little entrainment of the fluids. For the heavy third gas, Ξ is generally much lower than that for the light third gas (Fig. 13b). There is little mixing of the fluids relative to the entrainment of the fluids. When freeze-out occurs ($\frac{h}{\lambda} = 1.5$), there is a sharp reversal of the downward trend in Ξ because the interface is diffusing numerically and no longer growing. For all cases, there is no mix between the first and third gases.

6 Characterization of the dynamics at the small scales

To characterize the small-scale dynamics, we present the time evolution of the mass-weighted enstrophy in the whole domain,

$$\Omega = \int_S \rho\omega^2 \, \mathrm{d}S, \tag{11}$$

where $\omega = \nabla \times \mathbf{u}$ is the vorticity (Fig. 14). The curl is computed using the Gmsh Curl plugin which evaluates the derivatives of the Lagrange shape functions in each cell. The derivative operator for the present simulations is, therefore, second-order accurate. Ω varies with resolution for inviscid calculations but the overall trend, main features, and conclu-

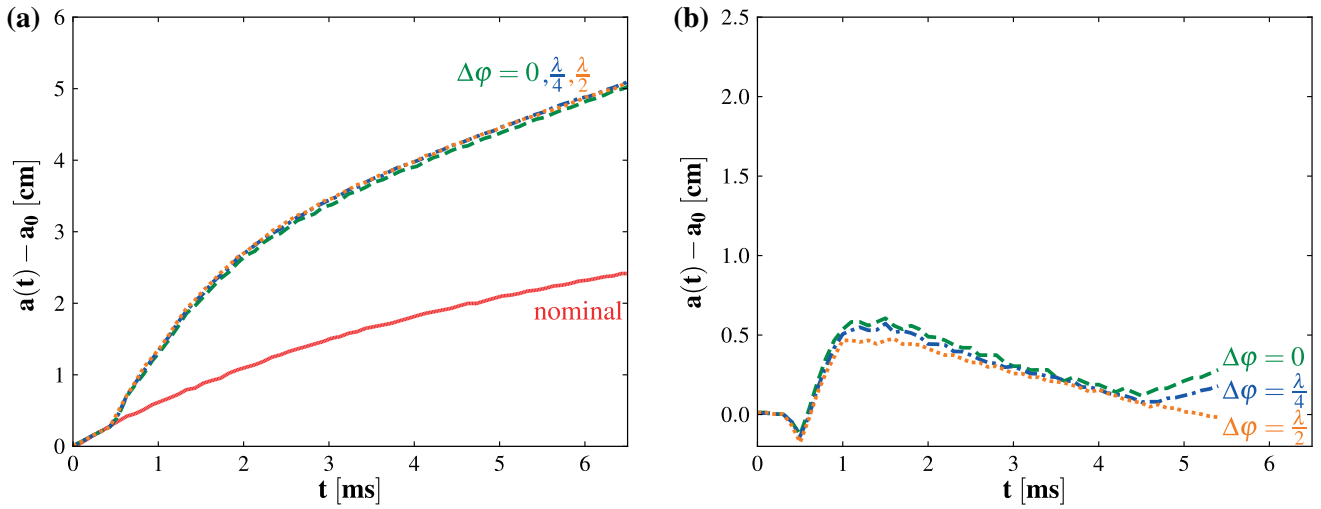

Fig. 16 Interface growth versus time for the baseline problem with a light third gas and $\frac{h}{\lambda} = 1$ for different phase misalignments. **a** Air-SF_6 interface. **b** SF_6-light third gas interface

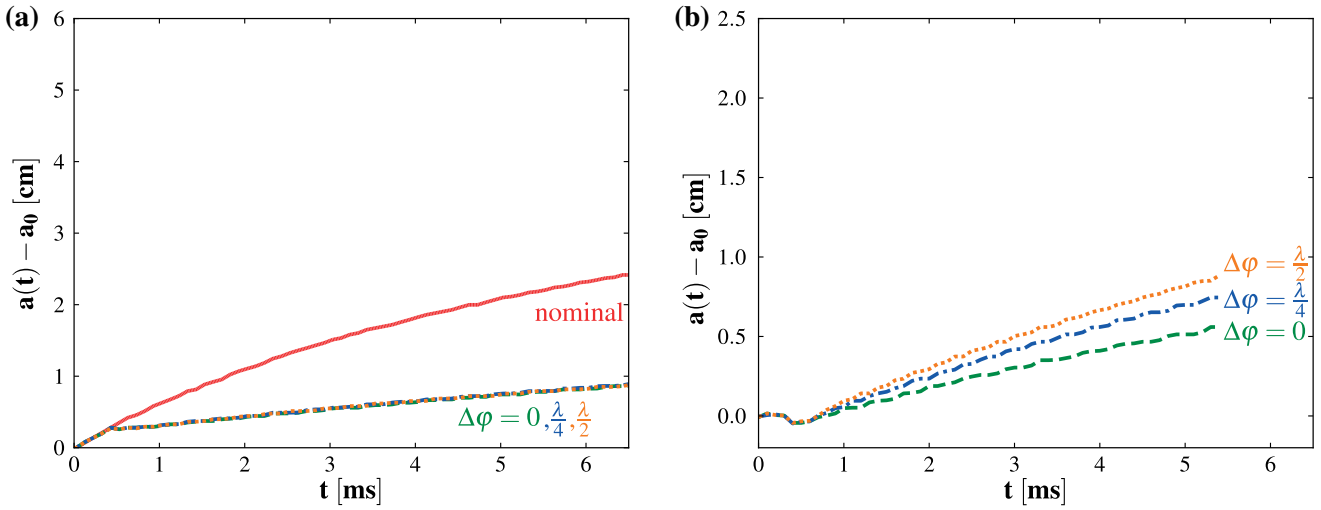

Fig. 17 Interface growth versus time for the baseline problem with a heavy third gas and $\frac{h}{\lambda} = 1$ for different phase misalignments. **a** Air-SF_6 interface. **b** SF_6-light third gas interface

sions remain unchanged when comparing to higher resolution simulations.

For both the heavy and the light third gas, the shock passage creates a jump in enstrophy due to baroclinic vorticity deposition at the interfaces and the generation of small scales. These small-scale features are more prevalent in the light third gas case, as indicated by the higher enstrophy (Fig. 14a). The increase in enstrophy by the reflected rarefaction waves as explained in Sect. 4.1 is clearly noticeable. For this case, increasing $\frac{h}{\lambda}$ further amplifies the small scales in the domain because the rarefaction interacts with a larger perturbed interface for a longer time.

For the heavy third gas case, the small-scale features are not as prevalent (Fig. 14b). The reflected shock interacts with a heavy-light interface, as opposed to the initial shock, and, therefore, the density gradient direction is opposite to that of the initial shock. As a result, this reflected shock generates baroclinic vorticity in the direction opposite to that of the initial shock, thereby reducing the amount of enstrophy in the domain (Fig. 14b). For this case, the enstrophy decreases as $\frac{h}{\lambda}$ increases because the perturbation is larger, amplifying the baroclinic vorticity generation of the reflected shock.

At the time of interaction with the second interface, the curvature of the shock wave depends on the distance it has traveled since the first interaction. For $\frac{h}{\lambda} = 0.5$, it retains some curvature upon interaction due to the first interface interaction. For large values of $\frac{h}{\lambda}$, the shock wave adopts a planar configuration by the time it reaches the second interface. This effect may account for the observed differences in the growths of the second interface (Fig. 11b) as a curved

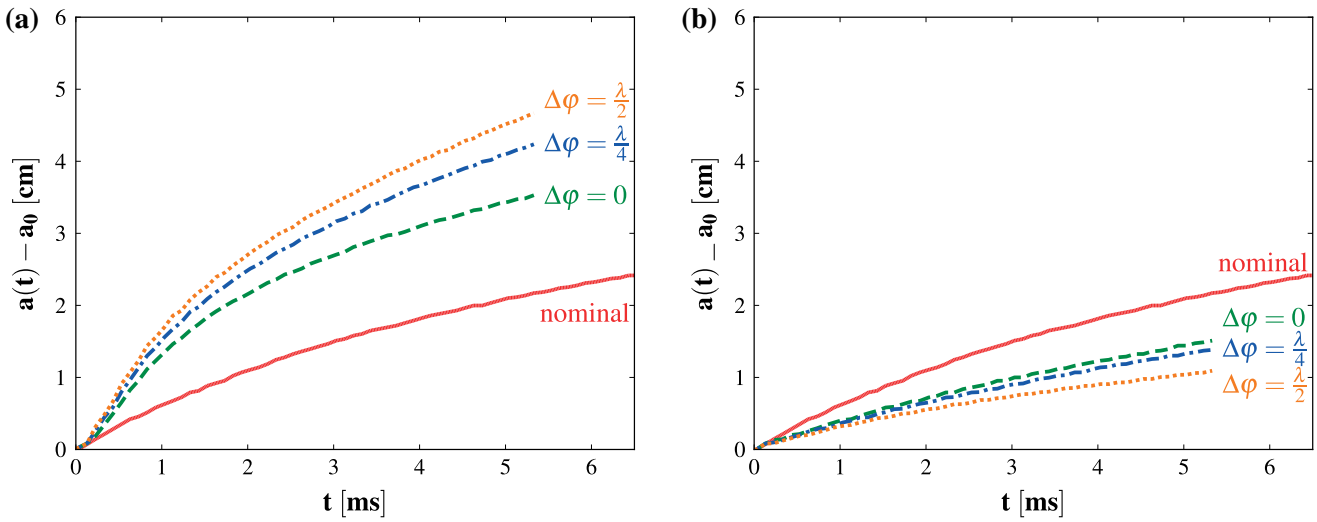

Fig. 18 Air-SF_6 interface growth versus time for the baseline problem, $\frac{h}{\lambda} = 0.5$ for different phase misalignments. **a** Light third gas. **b** Heavy third gas

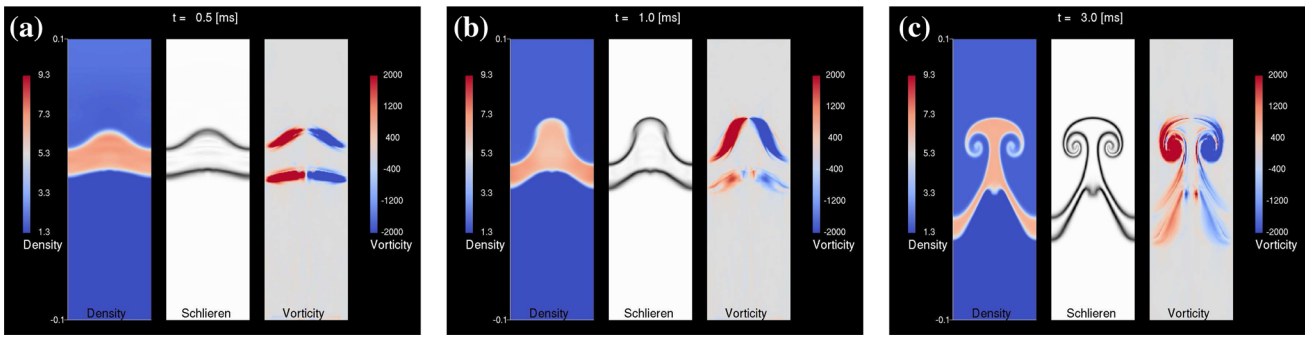

Fig. 19 Density (*left*), density gradient (numerical schlieren, *middle*) and vorticity (*right*) fields for the baseline problem and a light third gas ($\frac{h}{\lambda} = 0.5$ and $\Delta\varphi = \frac{\lambda}{2}$). **a** $t = 0.5$ ms. **b** $t = 1$ ms. **c** $t = 3$ ms

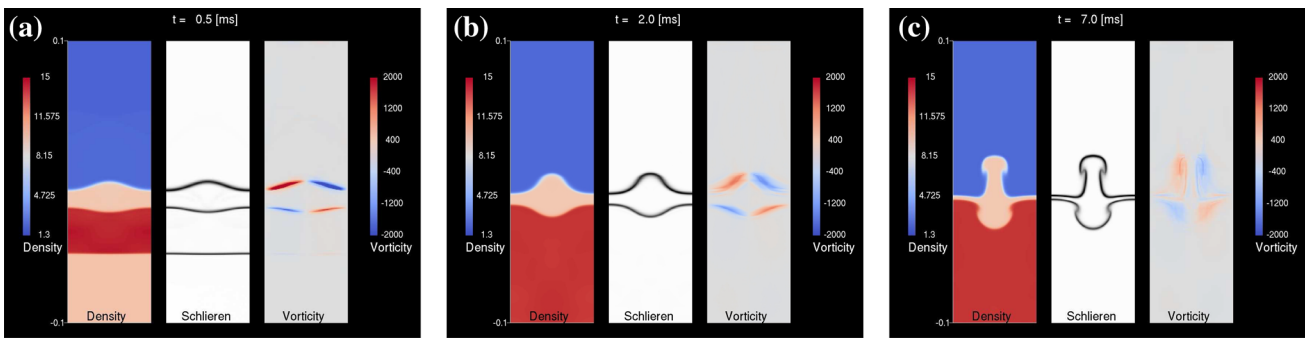

Fig. 20 Density (*left*), density gradient (numerical schlieren, *middle*) and vorticity (*right*) fields for the baseline problem with a heavy third gas ($\frac{h}{\lambda} = 0.5$ and $\Delta\varphi = \frac{\lambda}{2}$). **a** $t = 0.5$ ms. **b** $t = 2$ ms. **c** $t = 7$ ms

shock deposits more baroclinic vorticity at the interface. Higher enstrophy is in fact observed for $\frac{h}{\lambda} = 0.5$ while the other two distances have similar enstrophy profiles (Fig. 14b).

Calculating the energy of the small-scale motions can further expand our understanding of the energy at the small scales. We denote the average velocities in each horizontal cross section (spanwise direction) $\bar{u}$ and $\bar{v}$ and calculate the "turbulent kinetic energy" (TKE),[1]

$$\text{TKE} = \int_S \frac{1}{2}\rho\left[(u-\bar{u})^2 + (v-\bar{v})^2\right] \mathrm{d}S, \tag{12}$$

[1] Since the present simulations are two-dimensional, they cannot represent vortex stretching, and thus turbulence. By TKE, our intent is to describe the energy contained in the small scales.

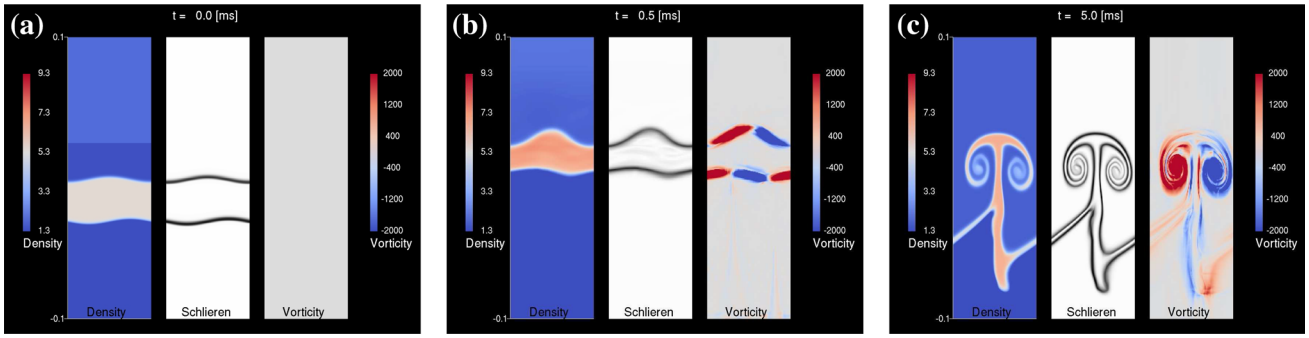

Fig. 21 Density (*left*), density gradient (numerical schlieren, *middle*) and vorticity (*right*) fields for the baseline problem with a light third gas ($\frac{h}{\lambda} = 0.5$ and $\Delta\varphi = \frac{\lambda}{4}$). **a** $t = 0$ ms. **b** $t = 0.5$ ms. **c** $t = 5$ ms

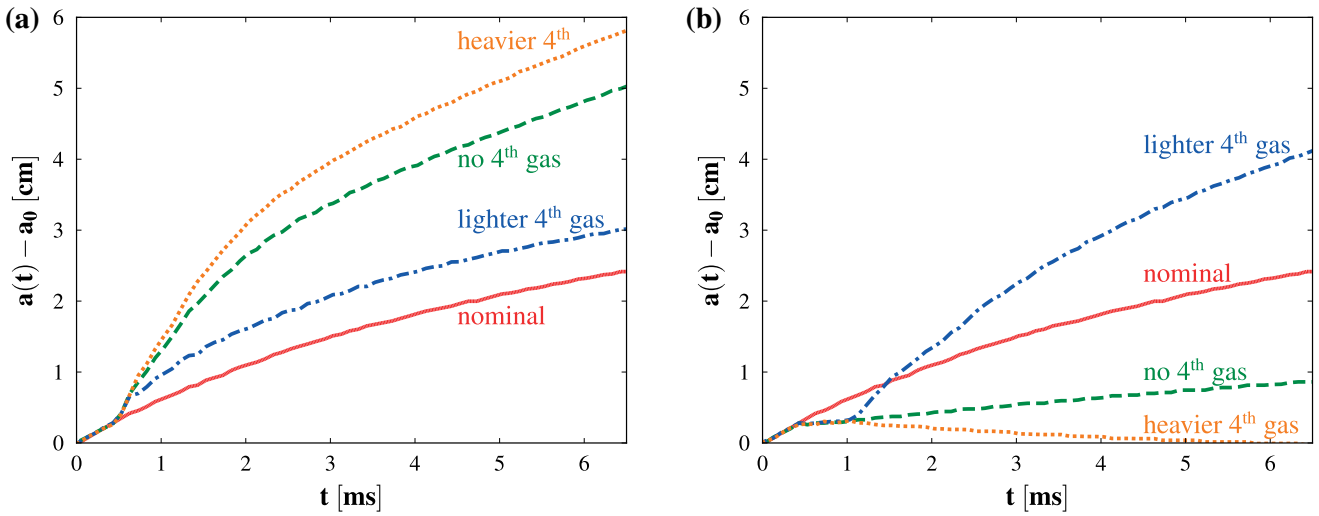

Fig. 22 Air-SF_6 interface growth versus time at $\frac{h}{\lambda} = 1$ with a fourth gas. **a** Light third gas. **b** Heavy third gas

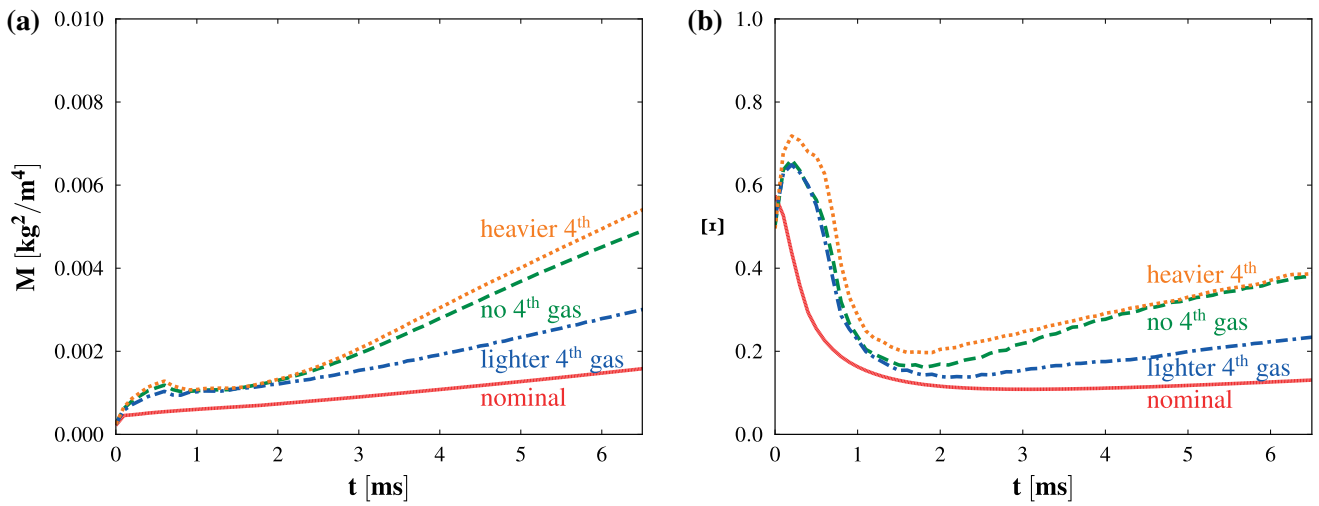

Fig. 23 Mixing metrics versus time for the light third gas case at $\frac{h}{\lambda} = 1$ with a fourth gas. **a** M. **b** Ξ

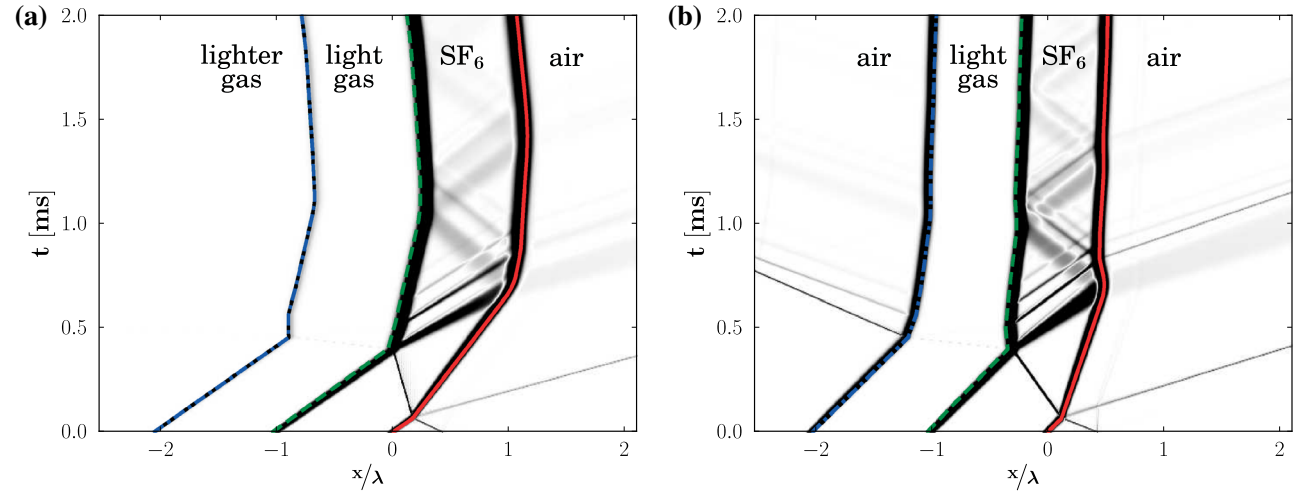

Fig. 24 Wave diagram from a one-dimensional simulation for the light third gas case with a fourth gas (initial shock coming from the right, $\frac{h}{\lambda} = 1$). *Solid red*: air-SF_6 interface; *dashed green*: SF_6-light third gas interface; *dashed-dot blue*: third-fourth gas interface. **a** Lighter fourth gas. **b** Heavier fourth gas

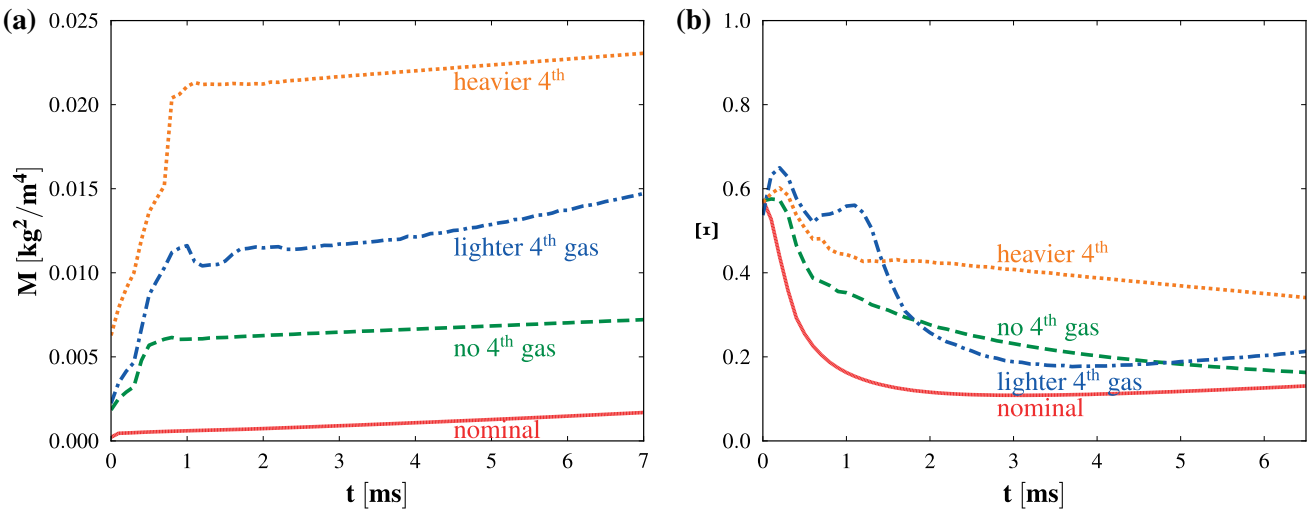

Fig. 25 Mixing metrics versus time for the heavy third gas case at $\frac{h}{\lambda} = 1$ with a fourth gas. **a** M. **b** Ξ

shown in Fig. 15. In the case of a light third gas, the initial shock and subsequent reflected rarefaction greatly increase the TKE in the domain with respect to the nominal case (Fig. 15a). This is due to the effect of the reflected rarefaction as detailed previously. However, for the heavy third gas case, the reflected shock causes a significant drop in TKE when it deposits vorticity in the opposite direction as the initial shock (Fig. 15b). For all cases, the slight decrease in enstrophy and TKE as a function of time is most likely due to numerical diffusion.

7 Effect of a phase difference between successive interfacial perturbations

In the problems to this point, we aligned the interfaces so that the initial perturbations are in phase. In this section, we investigate the effect of a "misalignment" on the perturbation growth. Because of the periodic nature of the problem, we restrict our study to a phase difference between the first and second interfaces $\Delta\varphi \in [0, \frac{\lambda}{2}]$. Specifically, we choose $\Delta\varphi = \frac{\lambda}{4}$ and $\frac{\lambda}{2}$ to compare to our baseline problem, where $\Delta\varphi = 0$.

The effect of the phase difference depends on the separation distance between the interfaces. When the interfaces are separated by a distance larger than $\frac{h}{\lambda} = 1$, the effect of $\Delta\varphi$ on the growth of either interface is negligible for both the light and heavy third gas cases (Figs. 16, 17). A slight asymmetry in the interface perturbation appears at late times but it is not very noticeable.

When the interfaces are closer to each other, e.g., $\frac{h}{\lambda} = 0.5$, the effect of $\Delta\varphi$ is more noticeable. For the light third gas case, the growth of the perturbations is enhanced (Fig. 18a).

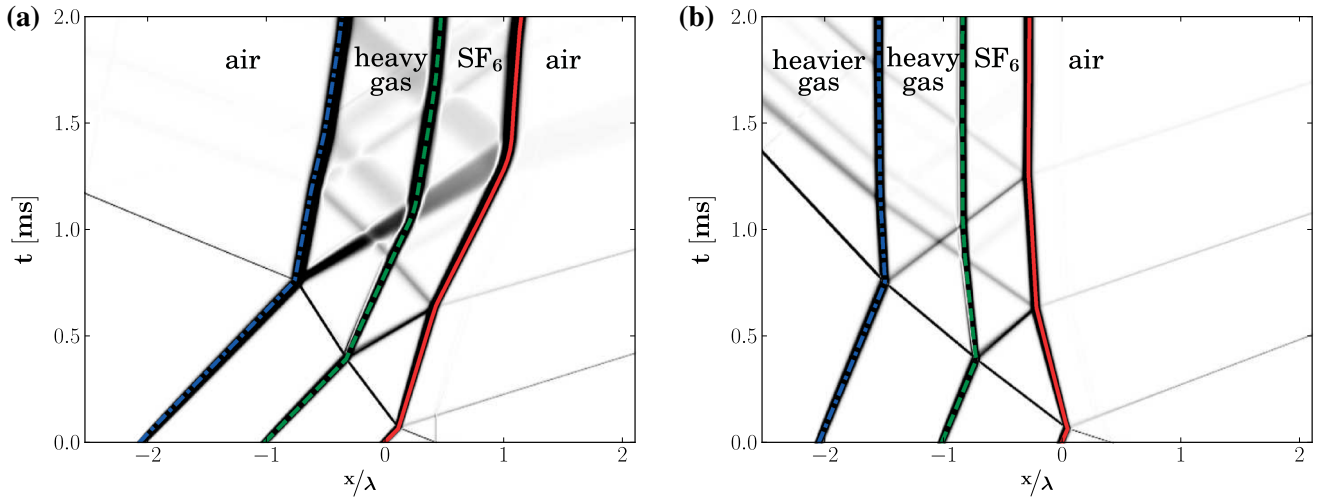

Fig. 26 Wave diagram from a one-dimensional simulation for the heavy third gas case with a fourth gas (initial shock coming from the right, $\frac{h}{\lambda} = 1$). *Solid red* air-SF_6 interface; *dashed green* SF_6-heavy third gas interface; *dashed-dot blue* third-fourth gas interface. **a** Lighter fourth gas. **b** Heavier fourth gas

When $\Delta\varphi = \frac{\lambda}{2}$, the vorticity is deposited in the same direction at both interfaces in each half of the domain (Fig. 19), thereby increasing the growth. This happens to a lesser extent for $\Delta\varphi = \frac{\lambda}{4}$. The case $\Delta\varphi = \frac{\lambda}{2}$ with a light third gas is analogous to the SF_6 gas curtain presented in [28] when the amplitudes of both interfaces are equal and opposite. Although our setup differs in the shock Mach number, initial perturbation amplitudes, and density ratios, [28] observes the same qualitative perturbation growth at both interfaces.

For the heavy third gas case, the growth diminishes as $\Delta\varphi$ increases (Fig. 18b). For $\Delta\varphi = \frac{\lambda}{2}$, the vorticity is deposited in the opposite direction at both interfaces in each half of the domain (Fig. 20), thereby decreasing the growth. This happens to a lesser extent for $\Delta\varphi = \frac{\lambda}{4}$. When $\Delta\varphi = \frac{\lambda}{4}$, there is a clear asymmetry in the evolution of the interfaces (Fig. 21). This behavior is due to asymmetric wave reflections and interface proximity effects.

8 Effect of a fourth gas

In this section, we study the effect of a fourth gas on the growth of the instability at the first interface. For the light third gas case, we use air as a heavier fourth gas and a gas with $\rho = 0.05\,\mathrm{kg/m^3}$ and $\gamma = \frac{5}{3}$ as a lighter gas. For the heavy third gas case, we use air as a lighter fourth gas and a gas with $\rho = 15\,\mathrm{kg/m^3}$ and $\gamma = \frac{5}{3}$ as a heavier gas.

The presence of a fourth gas can significantly change the growth. For a heavier fourth gas (Fig. 22a), growth of the first interface is enhanced. However, the amount of mix does not change significantly (Fig. 23). The heavier fourth gas has little effect on the mix. The wave dynamics are such that the reflected rarefactions are stronger and affect the interface for a longer period of time (Fig. 24). A lighter third gas suppresses the growth and the mixing as the reflected waves are weaker and their interactions decrease the baroclinic vorticity.

For the heavy third gas case, the growth is enhanced when using a lighter fourth gas (Fig. 22b). At the third interface, a rarefaction is reflected back towards the first interface (Fig. 26a), initiating a Rayleigh–Taylor growth phase at the first interface. When using a heavier fourth gas, a shock is reflected at the third interface, further amplifying the effect of the first reflected shock by depositing vorticity in the opposite direction as the initial shock and thereby decreasing the growth. Since the growth is small, Ξ increases because there is a small amount of entrained fluid relative to the mixed fluid (Fig. 25). For both the heavier and lighter fourth gas cases, M is larger because of the density weighing of the mass fractions. Though the perturbation growth for the heavier fourth gas case is smaller, there is increased mix in the domain.

9 Conclusions

In this work, we used a high-order accurate Discontinuous Galerkin method to simulate the interaction of a shock wave with successive interfaces separating different gases. In particular, we investigated the effect of the acoustic impedance (and density) of the third gas on the growth of the RMI at the

different interfaces. Through this study, we make the following conclusions:

- If the third gas is lighter than the second gas, the reflected rarefaction at the second interface amplifies the growth at the first interface for two main reasons: the reflected rarefaction deposits vorticity in the same direction as the incoming shock and the perturbation amplitude at the time of interaction with the rarefaction has grown. If the third gas is heavier, the reflected shock decreases the growth and tend to reverse the perturbation growth as the thickness of the second gas increases. This behavior is governed by Richtmyer–Meshkov (instantaneous acceleration of the interface) and Rayleigh–Taylor (acceleration of a heavy fluid into a light one) instabilities, which are both transient in this problem.
- The results strongly depend on the separation distance between the interfaces. We observed freeze-out in the case of a heavy third gas. This study supports the idea that perturbation growth may be controlled using rarefactions and shocks [27].
- We characterized fluid mixing through two different metrics. The light third gas resulted in higher fluid mixing relative to entrained unmixed fluid than the heavy third gas case.
- To represent the behavior at the small scales, we characterized the temporal evolution of enstrophy and energy of the small scales by relating this to the effect of the reflected waves.
- The phase difference between the perturbations does not affect the growth if the interfaces are far from each other. Because of baroclinic vorticity and interface proximity, the phase difference has a significant affect on the growth if the interfaces are initially close to each other.
- By adding a fourth gas, we can significantly increase the growth in a light-heavy-light-heavy or a light-heavy-heavier-light configuration. This effect is due to the RT-unstable phase of the growth induced by reflected rarefactions.

The present work presents an exploration of a small range of the parameter space; future exploration of the number of layers, gas properties and thicknesses, and amplitude properties are desirable to better understand this problem. This study forms the basis for further three-dimensional studies of randomly perturbed interfaces, transition to turbulence, and late-time mixing evolution. A more in-depth investigation of such a set-up may be beneficial to control perturbation growth in ICF.

Acknowledgments This research was supported in part by the DOE NNSA/ASC under the predictive Science Academic Alliance Program by Grant No. DEFC52-08NA28616, by ONR grant N00014-12-1-0751 under Dr. Ki-Han Kim, by NSF grant CBET 1253157, and through computational resources and services provided by Advanced Research Computing at the University of Michigan, Ann Arbor.

References

1. Abgrall, R.: How to prevent pressure oscillations in multicomponent flow calculations: a Quasi conservative approach. J. Comput. Phys. **125**(1), 150–160 (1996)
2. Adjerid, S., Devine, K.D., Flaherty, J.E., Krivodonova, L.: A posteriori error estimation for discontinuous Galerkin solutions of hyperbolic problems. Comput. Methods Appl. Mech. Eng. **191**(11–12), 1097–1112 (2002)
3. Adjerid, S., Massey, T.C.: Superconvergence of discontinuous Galerkin solutions for a nonlinear scalar hyperbolic problem. Comput. Methods Appl. Mech. Eng. **195**(25–28), 3331–3346 (2006)
4. Balakumar, B.J., Orlicz, G.C., Tomkins, C.D., Prestridge, K.P.: Simultaneous particle-image velocimetryplanar laser-induced fluorescence measurements of Richtmyer-Meshkov instability growth in a gas curtain with and without reshock. Phys. Fluids **20**(12), 124103 (2008)
5. Brouillette, M.: The Richtmyer-Meshkov instability. Ann. Rev. Fluid Mech. **34**(1), 445–468 (2002)
6. Cockburn, B., Hou, S., Shu, C.W.: The Runge-Kutta local projection discontinuous Galerkin finite element method for conservation laws IV: the multidimensional case. Math. Comput. **54**(190), 545–581 (1990)
7. Cockburn, B., Lin, G., Shu, C.W.: TVB Runge-Kutta local projection discontinuous Galerkin finite element method for conservation laws III: one-dimensional systems. J. Comput. Phys. **84**(1), 90–113 (1989)
8. Cockburn, B., Shu, C.W.: TVB Runge-Kutta local projection discontinuous Galerkin finite element method for conservation laws II: general framework. Math. Comput. **52**(186), 411–435 (1989)
9. Cockburn, B., Shu, C.W.: The local discontinuous Galerkin method for time-dependent convection-diffusion systems. SIAM J. Numer. Anal. **35**(6), 2440–2463 (1997)
10. Cockburn, B., Shu, C.W.: The Runge-Kutta discontinuous Galerkin method for conservation laws V: multidimensional systems. J. Comput. Phys. **141**(2), 199–224 (1997)
11. Collins, B.D., Jacobs, J.W.: PLIF flow visualization and measurements of the Richtmyer-Meshkov instability of an air/SF6 interface. J. Fluid Mech. **464**, 113–136 (2002)
12. Cook, A.W., Dimotakis, P.E.: Transition stages of RayleighTaylor instability between miscible fluids. J. Fluid Mech. **443**, 69–99 (2001)
13. Di Stefano, C.A., Malamud, G., Henry de Frahan, M.T., Kuranz, C.C., Shimony, A., Klein, S.R., Drake, R.P., Johnsen, E., Shvarts, D., Smalyuk, V.A., Martinez, D.: Observation and modeling of mixing-layer development in high-energy-density, blast-wave-driven shear flow. Phys. Plasmas **21**(5), 056306 (2014)
14. Drake, R.P.: High-Energy-Density Physics. Springer, Berlin (2006)
15. Geuzaine, C., Remacle, J.F.: Gmsh: a 3-D finite element mesh generator with built-in pre- and post-processing facilities. Int. J. Numer. Methods Eng. **79**(11), 1309–1331 (2009)
16. Goncharov, V.N., McKenty, P., Skupsky, S., Betti, R., McCrory, R.L., Cherfils-Clerouin, C.: Modeling hydrodynamic instabilities in inertial confinement fusion targets. Phys. Plasmas **7**(12), 5118–5139 (2000)
17. Hahn, M., Drikakis, D., Youngs, D.L., Williams, R.J.R.: RichtmyerMeshkov turbulent mixing arising from an inclined material interface with realistic surface perturbations and reshocked flow. Phys. Fluids **23**(4), 046101 (2011)
18. Henry de Frahan, M.T., Johnsen, E.: Discontinuous Galerkin method for multifluid Euler equations. In: 21st AIAA Comput.

Fluid Dyn. Conf., 2013–2595, pp. 1–12. American Institute of Aeronautics and Astronautics, Reston, Virginia (2013)
19. Henry de Frahan, M.T., Johnsen, E.: A new limiting procedure for discontinuous Galerkin methods applied to compressible multiphase flows with shocks and interfaces. J. Comput. Phys. **280**, 489–509 (2014). doi:10.1016/j.jcp.2014.09.030
20. Hill, D.J., Pantano, C., Pullin, D.I.: Large-eddy simulation and multiscale modelling of a Richtmyer-Meshkov instability with reshock. J. Fluid Mech. **557**(2006), 29–61 (2006)
21. Holmes, R.L., Dimonte, G., Fryxell, B., Gittings, M.L., Grove, J.W., Schneider, M., Sharp, D.H., Velikovich, A.L., Weaver, R.P., Zhang, Q.: Richtmyer-Meshkov instability growth: experiment, simulation and theory. J. Fluid Mech. **389**, 55–79 (1999)
22. Houim, R.W., Kuo, K.K.: A low-dissipation and time-accurate method for compressible multi-component flow with variable specific heat ratios. J. Comput. Phys. **230**(23), 8527–8553 (2011)
23. Kifonidis, K., Plewa, T., Scheck, L., Janka, H.T., Müller, E.: Nonspherical core collapse supernovae. Astron. Astrophys. **453**(2), 661–678 (2006)
24. Kutta, W.: Beitrag zur näherungsweisen Integration totaler Differentialgleichungen. Zeitschr. fr Math. u. Phys. **46**, 435–453 (1901)
25. Landen, O.L., Benedetti, R., Bleuel, D., Boehly, T.R., Bradley, D.K., Caggiano, J.A., Callahan, D.A., Celliers, P.M., Cerjan, C.J., Clark, D., Collins, G.W., Dewald, E.L., Dixit, S.N., Doeppner, T., Edgell, D., Eggert, J., Farley, D., Frenje, J.A., Glebov, V., Glenn, S.M., Glenzer, S.H., Haan, S.W., Hamza, A., Hammel, B.A., Haynam, C.A., Hammer, J.H., Heeter, R.F., Herrmann, H.W., Hicks, D.G., Hinkel, D.E., Izumi, N., Gatu Johnson, M., Jones, O.S., Kalantar, D.H., Kauffman, R.L., Kilkenny, J.D., Kline, J.L., Knauer, J.P., Koch, J.A., Kyrala, G.A., LaFortune, K., Ma, T., Mackinnon, A.J., Macphee, A.J., Mapoles, E., Milovich, J.L., Moody, J.D., Meezan, N.B., Michel, P., Moore, A.S., Munro, D.H., Nikroo, A., Olson, R.E., Opachich, K., Pak, A., Parham, T., Patel, P., Park, H.S., Petrasso, R.P., Ralph, J., Regan, S.P., Remington, B.A., Rinderknecht, H.G., Robey, H.F., Rosen, M.D., Ross, J.S., Salmonson, J.D., Sangster, T.C., Schneider, M.B., Smalyuk, V., Spears, B.K., Springer, P.T., Suter, L.J., Thomas, C.A., Town, R.P.J., Weber, S.V., Wegner, P.J., Wilson, D.C., Widmann, K., Yeamans, C., Zylstra, A., Edwards, M.J., Lindl, J.D., Atherton, L.J., Hsing, W.W., MacGowan, B.J., Van Wonterghem, B.M., Moses, E.I.: Progress in the indirect-drive National Ignition Campaign. Plasma Phys. Control. Fusion **54**(12), 124026 (2012)
26. Latini, M., Schilling, O., Don, W.S.: Effects of WENO flux reconstruction order and spatial resolution on reshocked two-dimensional Richtmyer-Meshkov instability. J. Comput. Phys. **221**(2), 805–836 (2007)
27. Lindl, J.: Development of the indirect-drive approach to inertial confinement fusion and the target physics basis for ignition and gain. Phys. Plasmas **2**(11), 3933–4024 (1995)
28. Mikaelian, K.O.: Numerical simulations of Richtmyer-Meshkov instabilities in finite-thickness fluid layers. Phys. Fluids **8**(5), 1269–1292 (1996)
29. Motl, B., Oakley, J., Ranjan, D., Weber, C., Anderson, M., Bonazza, R.: Experimental validation of a Richtmyer-Meshkov scaling law over large density ratio and shock strength ranges. Phys. Fluids **21**(12), 126102 (2009)
30. Movahed, P., Johnsen, E.: Numerical simulations of the Richtmyer-Meshkov instability with reshock. In: 20th AIAA Comput. Fluid Dyn. Conf., 2011–3689, pp. 1–12. American Institute of Aeronautics and Astronautics, Reston, Virigina (2011)
31. Movahed, P., Johnsen, E.: A solution-adaptive method for efficient compressible multifluid simulations, with application to the Richtmyer-Meshkov instability. J. Comput. Phys. **239**, 166–186 (2013)
32. Richtmyer, R.D.: Taylor instability in shock acceleration of compressible fluids. Commun. Pure Appl. Math. **13**(2), 297–319 (1960)
33. Roe, P.L.: Approximate Riemann solvers, parameter vectors, and difference schemes. J. Comput. Phys. **43**(2), 357–372 (1981)
34. Schilling, O., Latini, M., Don, W.: Physics of reshock and mixing in single-mode Richtmyer-Meshkov instability. Phys. Rev. E **76**(2), 026319 (2007)
35. Shankar, S.K., Lele, S.K.: Numerical investigation of turbulence in reshocked RichtmyerMeshkov unstable curtain of dense gas. Shock Waves **24**(1), 79–95 (2013)
36. Taylor, G.: The instability of liquid surfaces when accelerated in a direction perpendicular to their planes. I. Proc. R. Soc. A Math. Phys. Eng. Sci. **201**(1065), 192–196 (1950)
37. Vetter, M., Sturtevant, B.: Experiments on the Richtmyer-Meshkov instability of an air/SF6 interface. Shock Waves **4**(5), 247–252 (1995)
38. Weber, C., Haehn, N., Oakley, J., Rothamer, D., Bonazza, R.: Turbulent mixing measurements in the Richtmyer-Meshkov instability. Phys. Fluids **24**(7), 074105 (2012)